Eurographics Workshop on Visual Computing for Biology and Medicine (2017)
I. Hotz, D. Merhof, and C. Rieder (Editors)

Multi-fiber Estimation and Tractography for Diffusion MRI using mixture of Non-central Wishart Distributions

Snehlata Shakya[1], Xuan Gu[1,2], Nazre Batool[3], Evren Özarslan[1,2] and Hans Knutsson[1,2]

[1]Department of Biomedical Engineering, Linköping University, Linköping, Sweden
[2]Center for Medical Image Science and Visualization, Linköping University, Linköping, Sweden
[3]KTH Royal Institute of Technology, Stockholm, Sweden

Abstract

Multi-compartmental models are popular to resolve intra-voxel fiber heterogeneity. One such model is the mixture of central Wishart distributions. In this paper, we use our recently proposed model to estimate the orientations of crossing fibers within a voxel based on mixture of non-central Wishart distributions. We present a thorough comparison of the results from other fiber reconstruction methods with this model. The comparative study includes experiments on a range of separation angles between crossing fibers, with different noise levels, and on real human brain diffusion MRI data. Furthermore, we present multi-fiber visualization results using tractography. Results on synthetic and real data as well as tractography visualization highlight the superior performance of the model specifically for small and middle ranges of separation angles among crossing fibers.

1. Introduction

Multi-compartmental models solve the multi-fiber heterogeneity where MR signal can be represented as the weighted sum of signals from multiple compartments within a voxel. Bi-exponential diffusion MRI was first proposed by Inglis et al. [IBB*01] and Tuch et al. [TRW*02] employed it to resolve multiple fiber populations. The mixture of central Wishart distributions (*MoCW*) and the mixture of Hyper-spherical von Mises-Fisher Distributions models were proposed by Jian et al. [JVO*07] and Kumar et al. [KVW*09] respectively. In our previous work [SGB*17], we proposed a mixture of non-central Wishart distributions (*MoNCW*) model and presented comparative results with other multi-compartmental models based on the mixture of probability distributions. *MoNCW* is theoretically similar to Jian et al.'s *MoCW* model and adds a non-centrality parameter to the Wishart distribution.

In this work, we extend our prior work [SGB*17] by presenting detailed experiments on comparing the *MoNCW* model with state-of-the-art algorithms [DCRD*14] in Section 3. The *MoNCW* model exhibits improved performance over other algorithms for small and middle ranges of separation angles between crossing fibers. Furthermore, we present the results of tractography using *MoNCW* model in section 3.3. Section 3.4 includes results with real data where tractography results are compared with the multi-tensor model. The *MoNCW* model shows visually promising results for crossing fiber regions as compared with other methods.

2. Theory

In this section, we present a brief theoretical background of the *MoNCW* model. The interested reader is referred to [SGB*17] for theoretical details of different multi-compartment models and the parameter estimation of the model.

In probabilistic framework, MRI signal decay can be given as:

$$S = S_0 \int_{\mathbf{P}_n} f(\mathbf{D}) \exp(-b\mathbf{g}^T\mathbf{D}\mathbf{g}) d\mathbf{D}, \quad (1)$$

$$= S_0 \int_{\mathbf{P}_n} f(\mathbf{D}) \exp(-\mathrm{trace}(\mathbf{B}\mathbf{D})) d\mathbf{D} = S_0 \mathbf{L}_f(\mathbf{B}), \quad (2)$$

where $\mathbf{P}_n$ is the manifold of $n \times n$ symmetric positive-definite matrices, S_0 is the signal in the absence of any diffusion weighting gradient, $\mathbf{D}$ is the apparent diffusion tensor and $\{\mathbf{B} = b\mathbf{g}\mathbf{g}^T; \mathbf{B} \in \mathbf{P}_n\}$ with $b = (\gamma\delta\mathbf{G})^2 t$ is the 'b-value', γ is the gyromagnetic ratio, δ is the diffusion gradient duration and t is the effective diffusion time. G and $\mathbf{g}$ are the magnitude and direction of the diffusion sensitizing gradient $\mathbf{G}$ and $f(\mathbf{D})$ is a density function on the space of $\mathbf{P}_n$ with respect to some measure $d\mathbf{D}$. $\mathbf{L}_f$ is the standard Laplace transform of a function f.

The Laplace transform of non-central Wishart distribution, $W_n(p, \Sigma, \Omega)$, is given as follows [May13] (Here, we omit the definition of W_n for brevity):

$$\int \exp(-\mathrm{trace}(\Theta u)) W_n(p, \Sigma, \Omega) du = \left|I_n + \Theta\Sigma\right|^{-p} \times \exp\left[-\mathrm{trace}(\Theta(I_n + \Theta\Sigma)^{-1}\Omega)\right], \quad (3)$$

DOI: 10.2312/vcbm.20171244

where $(\Theta + \Sigma^{-1}) \in \mathbf{P}_n$. The expected value of the non-central Wishart distribution is given as $p\Sigma + \Omega$ [dW72]. To resolve intra-voxel multi-fiber heterogeneity, we propose a (weighted) *MoNCW* model as a probabilistic multi-compartmental model for **D** [SGB*17] and Eqn. 3 becomes:

$$\frac{S(\mathbf{q})}{S_0} = \sum_{i=1}^{N} w_i (1 + \text{trace}(\mathbf{B}\Sigma_i))^{-p} \exp\left[-\text{trace}(\mathbf{B}(I_n + \mathbf{B}\Sigma_i)^{-1}\Omega_i)\right], \tag{4}$$

where w_i are the mixture weights. If p_i's, Σ_i's and Ω_i's are fixed, the above system of linear equations can be solved to determine w_i.

We fix the value of $p = 2$ and the eigenvalues of $\mathbf{D}_i = p\Sigma_i + \Omega_i$ to $(\lambda_1, \lambda_2, \lambda_3) = (1.5, 0.4, 0.4)\ \mu m^2/ms$ for each i, as assumed by Jian et al. [JVO*07]. We choose the non-centrality parameter, $\Omega_i = \alpha \mathbf{D}_i$ with $\alpha = 0.99$ [SGB*17]. Finally, Eqn. 4 leads to a linear system of equations, $\mathbf{Aw} = \mathbf{s}$, where $\mathbf{s} = S(\mathbf{q})/S_0$ is the normalized signal vector, $\mathbf{w}$ is the vector of unknown weights and $\mathbf{A}$ is the matrix with elements $\{A_{ji}; j = 1, 2, ..., K, i = 1, 2, ..., N\}$ given as,

$$A_{ji} = \left[1 + \text{trace}(\mathbf{B}_j\Sigma_i)\right]^{-p} \exp\left[-\text{trace}\left\{\mathbf{B}_j\ (I_n + \mathbf{B}_j\Sigma_i)^{-1}\Omega_i\right\}\right]. \tag{5}$$

The matrix $\mathbf{A}$ needs to be calculated once. The total number of diffusion weighted measurements is denoted by K. To avoid an underdetermined system, the condition $N \geq K$ has to be met. We employed the non-negative least square (NNLS, L-2 norm) to estimate $\mathbf{w}$. Results were compared in terms of 'angular accuracy' $\bar{\theta}$ defined as follows [DCRD*14]:

$$\bar{\theta} = \frac{180}{\pi} \arccos(|\mathbf{d}_{true} \cdot \mathbf{d}_{estimated}|)$$

where the vectors $\mathbf{d}_{true}$ and $\mathbf{d}_{estimated}$ are true and estimated fiber orientations, respectively, and $(\cdot)$ represents the dot product.

3. Results and Discussion

In this section we present a comparative study with other recently reported reconstruction methods. For all simulation cases, the b-value was chosen as 1500 s/mm^2. The values of N and K were chosen as 321 and 81 to generate synthetic data. These values were chosen to make a fair comparison with the *MoCW* model.

3.1. Experiments with changing noise levels

We used the adaptive kernel [BJV09] and the mixture of Gaussian model (*MoG*) [DCRD*14] to generate synthetic data. We then reconstructed fiber orientations with the *MoCW* and *MoNCW* models. We performed simulations for two-fiber case with the angle of separation increasing from 0° to 90° with the increment of 1°. The weights for these fibers were kept equal to 0.5. Two different levels of Rician noise were added to the data. Experiments were repeated 10 times for each angular configuration. Figure 1 shows angular accuracy when SNR was 30. The plot on top includes the comparison of 20 reconstruction algorithms as reported by Daducci et al. [DCRD*14]. The bottom plot shows results with the *MoCW* and *MoNCW* models on synthetic data generated using both the

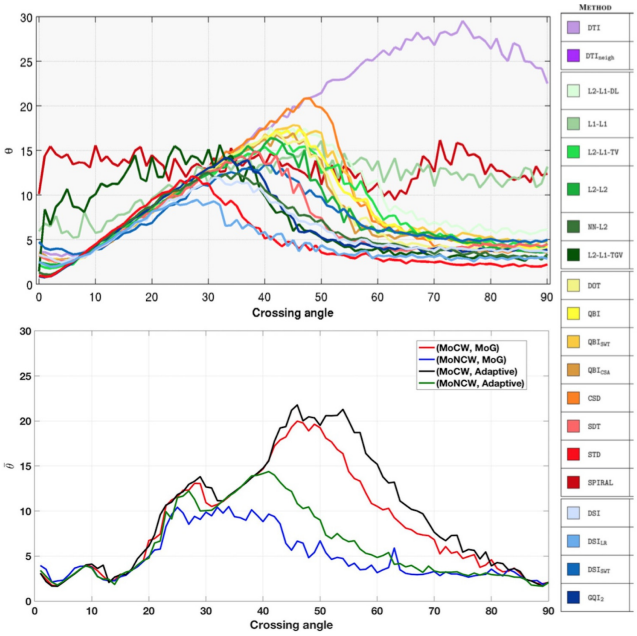

Figure 1: *Angular accuracy (in degrees) with increasing separation angles between two crossing fibers. Top: comparison of 20 reconstruction algorithms, reproduced from [DCRD*14]. Bottom: plots obtained from the MoCW and MoNCW models, SNR=30.*

MoG and adaptive kernel methods. The angular error is low for the *MoNCW* model for both datasets. However, we focused on the *MoG* model for the comparison as Daducci et al. [DCRD*14] used the same model to generate their data. The performance of the *MoNCW* model is better than many of the 20 other algorithms and is comparable to the diffusion spectrum imaging based on Lucy-Richardson deconvolution (DSI_{LR}) which was shown to be the best in terms of angular accuracy. For example, the average angular accuracy values for the *MoNCW* model (vs. DSI_{LR} model) were observed to be 5° (vs. 6°), 7° (vs. 5°) and 3° (vs. $3-4°$) for separation angle ranges of $0° - 30°$, $31° - 60°$ and $61 - 90°$ respectively.

Next we increased the noise level in the data to assess the stability of the *MoNCW* model. The plots for angular accuracy with a noise level of SNR=10 are shown in Fig. 2. Most of the reconstruction algorithms become unstable in the presence of high noise except the DSI_{LR} model. The *MoNCW* model also exhibits small fluctuations in the angular accuracy curve. However, it performs better than most of the other 19 reconstruction algorithms. In this case the average angular accuracy values for the *MoNCW* model (vs. DSI_{LR} model) were observed to be 6.8° (vs. $6 - 7°$), 11.2° (vs. $8 - 9°$) and 7.6° (vs. $6 - 7°$) for the separation angle ranges of $0° - 30°$, $31° - 60°$ and $61 - 90°$ respectively. The next best performing model was based on diffusion spectrum imaging, namely 3D Stationary Wavelet Transform (DSI_{SWT}), where the average angular accuracy for the three separation angle ranges were $6 - 7°$, $13 - 14°$ and 8°. Hence, the *MoNCW* model performed better than the second best DSI_{SWT} model in the presence of high levels of noise. One noticeable point is that *DSI* based models are developed

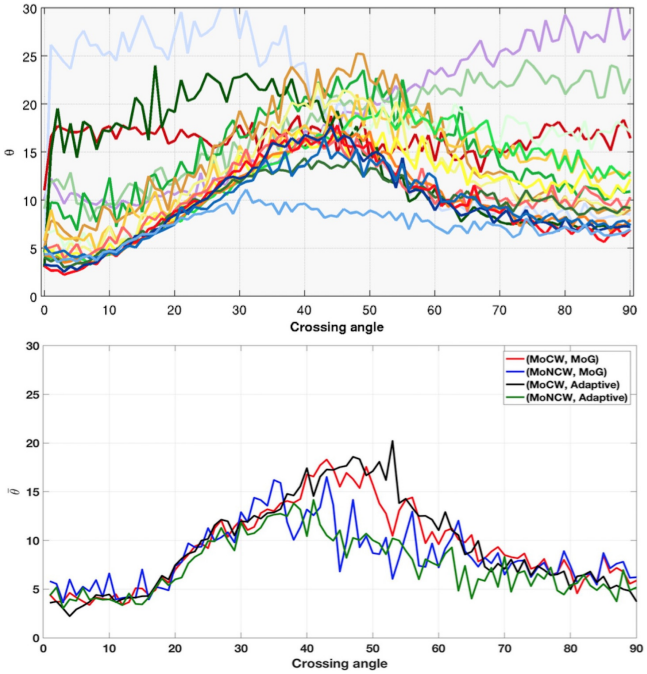

Figure 2: *Angular accuracy (in degrees) with increasing separation angle between two crossing fibers. Top image, which features the same coloring scheme as in Fig. 1, is comparison of 20 reconstruction algorithms [DCRD*14] and bottom image shows plots obtained from MoCW and MoNCW models, SNR=10.*

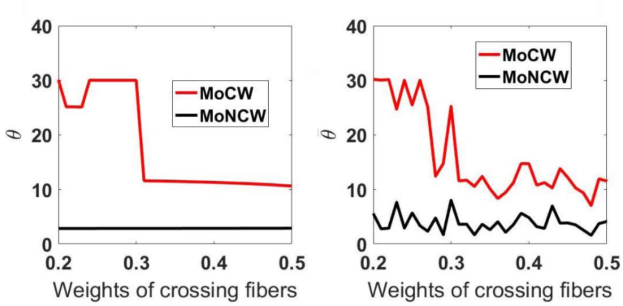

Figure 3: *Angular accuracy (in degrees) with changing weights. Left: no noise, Right: SNR=30. MoCW and MoNCW models are compared using synthetic data generated from the MoG model.*

for multi-shell data and our simulations are based on single shell data. Therefore, *DSI* based models are expected to perform better.

3.2. Experiments with changing weights of fibers

Next, we performed simulations by changing the weights of two crossing fibers in the test data generation. The crossing angle between two fibers was kept fixed at 60° arbitrarily while the fiber weights were changed from 0.2 to 0.5 with an increment of 0.01. Angular accuracy plots for this experiment are shown in Fig. 3. In this case, we compared results with the *MoCW* model only as there was no similar study available to compare results with the aforementioned other 20 algorithms. The left plot shows outcomes from the *MoCW* and *MoNCW* models in the absence of noise, and the right plot is in the presence of noise of SNR=30. The error with the *MoCW* model is significantly higher when the fiber weight is less than 0.3 as the model fails to reconstruct fibers with less weight. It is nearly 4° when the fibers share equal weights while it fluctuates between 2° an 8° for other weights in the *MoNCW* model. This error, however, ranges from 6° to 30° with the *MoCW* model.

3.3. Experiments on crossing tensor field

In this section, we present the simulation of crossing fiber field with known fiber orientations. For visualization of fibers, streamline tracing is the most commonly used technique which is also known as fiber tracking [MvZ02] or tractography [BPP*00]. This technique uses diffusion tensors of each voxel to follow the axonal tracts in 3D from voxel to voxel. We used open-source software toolkit Camino [CBNG*06] to perform tractography. This tool uses compartmental models, multi-fiber and HARDI reconstruction techniques to find major fiber orientations within a voxel. We performed tractography utilizing fiber orientations obtained from the *MoNCW* model. The seed points to initiate the streamlines were defined from the fractional anisotropy (FA) map and the *ITK snap* [YPH*06] imaging tool was used to define a region of interest (ROI). Fractional anisotropy threshold also needs to be defined to terminate fibers that enter a voxel with anisotropy lower than the specified threshold.

Fig. 4 presents the original crossing fiber field. The left image shows the discrete representation of fibers using spherical harmonics of order 8 while the right image shows the continuous representation of fibers through tractography. The separation angle between two fibers in crossing region is 45°. For our simulation, we chose seed points to be parallel to the fibers running from left to right and saved this region of interest in NIfTI (.nii) format. Next, the selected region and the outcomes from the *MoCW* and *MoNCW* models were used to perform tractography and the streamlines were visualized in a tool called *Paraview* [AGL05]. The results are displayed in Fig. 5. The middle left image is reconstructed with the *MoCW* model where, in the crossing region (bottom left of the image), the recovered single fiber can be observed to be an approximate average of the two fiber orientations. Whereas in the middle right image (reconstructed with the *MoNCW* model), in the crossing region (bottom right of the image) the presence of two distinct fibers can be observed. Although the *MoNCW* model was able to capture the presence of two crossing fibers, the error in both fiber orientations appeared to be high. It could be due to the interpolation of fiber orientations while computing streamlines. Therefore, we also present fiber orientations using spherical harmonics. The top left image is the reconstruction with the *MoCW* model and the top right image is with the *MoNCW* model which clearly shows that the latter exhibits less error.

3.4. Experiments on real data

Finally, we applied the *MoNCW* model on real human brain data. We used a two-shell healthy DWI-MRI dataset from MyConnec-

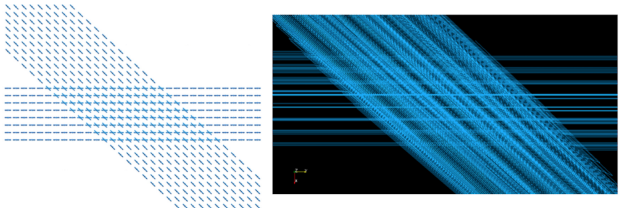

Figure 4: *Visualization of true fiber orientations of a crossing field Left: spherical harmonics, Right: tractography.*

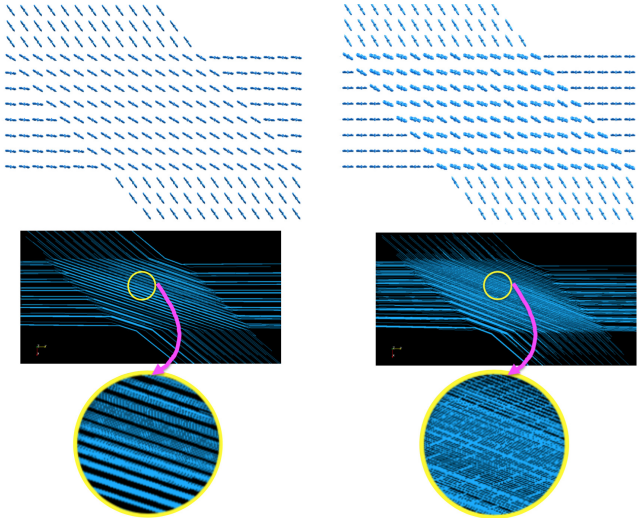

Figure 5: *Top left and right images are reconstructions with the MoCW and MoNCW models respectively (display with spherical harmonics); Bottom left and right images are displayed with tractography.*

tome project [LGA*15] (myconnectome.org). The dataset was collected for multiband EPI sequence for two b-values of 1000 and 2000 s/mm^2. More detailed information about the experiment can be found in [SGB*17]. Here, we present the 42^{nd} slice, where spherical harmonics are used to visualize fiber orientations. This result is shown in Fig. 6 and also reported earlier [SGB*17]. Fractional anisotropy (FA) is calculated using FSL software [JBB*12] and computed displacement probability maps are superimposed on this FA map. These images show that the *MoNCW* model is able to extract the orientations of anisotropic fibers in the regions of corpus callosum splenium (left) and of corpus callosum genu (right) of the human brain.

Next, we conducted tractography for the same data from the MyConnectome project [LGA*15]. The ROI of the seed points lies in the middle of the corpus callosum and is shown in the top image of Fig. 7. The bottom image is the outcome of tractography with input from the *MoNCW* model. The anisotropy threshold was set to 0.2 for this case. As the ROI is large, the number of streamlines is very large and hence it is difficult to make any observation. Therefore, we experimented further with a smaller ROI and larger threshold value. Fig. 8A shows the sagittal plane of the anisotropy

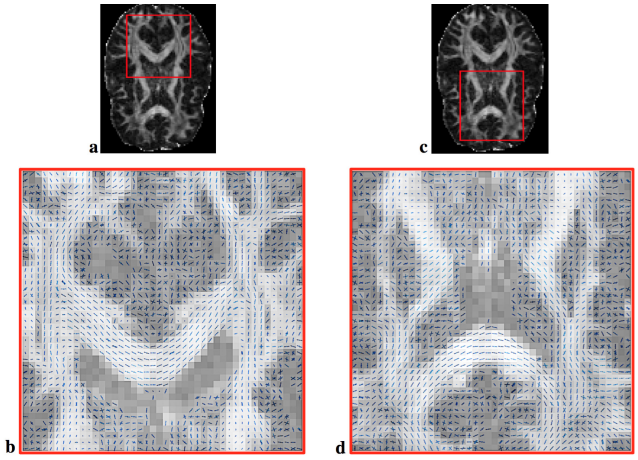

Figure 6: *Probability maps for corpus callosum splenium (lower left) and genu (lower right) of healthy human brain overlaid on FA maps. Images on top, (a) and (c) are the FA maps of whole brain slice with selected regions displayed in (b) and (d).*

map with selected ROI and Fig. 8B shows the coronal plane with the same ROI as in image A. Tractography is performed with this ROI and an anisotropy threshold value of 0.68. Fig. 8C shows the result with the *MoNCW* model and Fig. 8D shows the outcome by using Camino's built-in two tensor (positive definite) model [SA14] and [ALE05]. We highlight a region in the pink circle in image B and compare images in panels C and D. It can be observed that the region of fiber bifurcation is visible with the *MoNCW* model but is invisible with the two tensor model.

4. Conclusions

In this paper, we presented detailed experiments on mixture of non-central Wishart distributions. Our experiments demonstrate that the model's performance is comparable and, in some cases, better than the state-of-the-art algorithms specially when the separation angle between two fibers is in the middle range$(25^\circ - 65^\circ)$. We performed some simulations and tested our method for real human brain data. We compared tractography results with multi-tensor model utilizing Camino software and showed that the *MoNCW* model performs better for the crossing regions.

Acknowledgement

This research is a part of the project "Seeing Organ Function" funded by "The Knut and Alice Wallenberg Foundation". E. Ö. acknowledges support by Linköping University Center for Industrial Information Technology (CENIIT).

References

[AGL05] AHRENS J., GEVECI B., LAW C.: *ParaView: An End-User Tool for Large Data Visualization*. Visualization Handbook, Elsevier, Jan 2005, pp. 717–731. 3

[ALE05] ALEXANDER D. C.: Multiple-fiber reconstruction algorithms for diffusion MRI. *Annals of the New York Academy of Sciences 1064*, 1 (2005), 113–133. 4

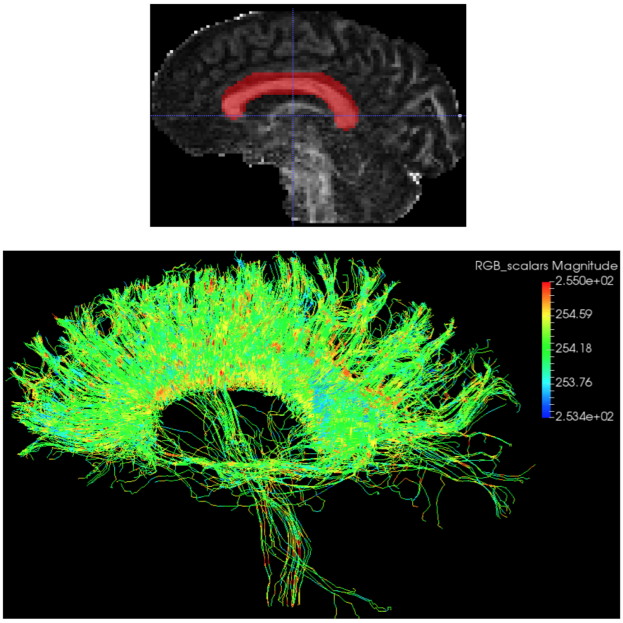

Figure 7: *Tractography: (Top) FA maps of human brain with the selected ROI for seeding, (bottom) basic streamlines for the given ROI with the MoNCW model.*

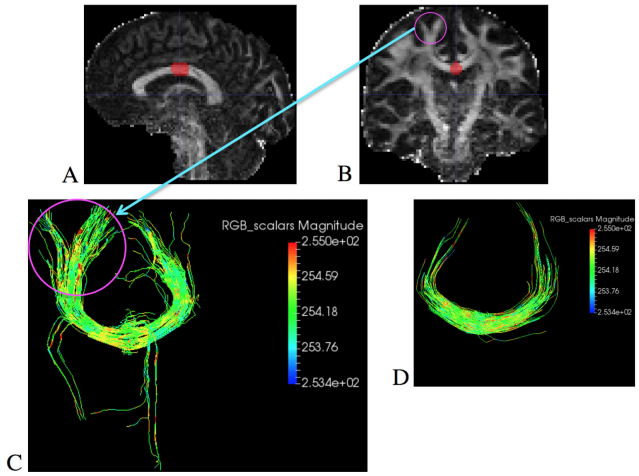

Figure 8: *Tractography: (Top) FA maps of human brain with the selected ROI for seeding: A is the sagittal plane, B is coronal plane with the same ROI as in image A. Bottom : C, is the display of basic streamlines for the given ROI with the MoNCW model (bottom left) and D is with the multi-tensor model (bottom right).*

[BJV09] BARMPOUTIS A., JIAN B., VEMURI B. C.: *Adaptive Kernels for Multi-fiber Reconstruction*. Springer Berlin Heidelberg, 2009, pp. 338–349. 2

[BPP*00] BASSER P. J., PAJEVIC S., PIERPAOLI C., DUDA J., ALDROUBI A.: In vivo fiber tractography using DT-MRI data. *Magnetic Resonance in Medicine 44*, 4 (2000), 625–632. 3

[CBNG*06] COOK P. A., BAI Y., NEDJATI-GILANI S., SEUNARINE K. K., HALL M. G., PARKER G. J., ALEXANDER D. C.: Camino: Open-source diffusion-MRI reconstruction and processing. In *14th scientific meeting ISMRM* (2006), p. 2759. 3

[DCRD*14] DADUCCI A., CANALES-RODRIGUEZ E. J., DESCOTEAUX M., GARYFALLIDIS E., GUR Y., LIN Y. C., MANI M., MERLET S., PAQUETTE M., RAMIREZ-MANZANARES A., REISERT M., RODRIGUES P. R., SEPEHRBAND F., CARUYER E., CHOUPAN J., DERICHE R., JACOB M., MENEGAZ G., PRCKOVSKA V., RIVERA M., WIAUX Y., THIRAN J. P.: Quantitative comparison of reconstruction methods for intra-voxel fiber recovery from diffusion MRI. *IEEE Transactions on Medical Imaging 33*, 2 (Feb 2014), 384–399. 1, 2, 3

[dW72] DE WAAL D. J.: On the expected values of the elementary symmetric functions of a noncentral wishart matrix. *Ann. Math. Statist. 43*, 1 (02 1972), 344–347. 2

[IBB*01] INGLIS B. A., BOSSART E. L., BUCKLEY D. L., WIRTH E. D., .MARECI T. H.: Visualization of neural tissue water compartments using biexponential diffusion tensor mri. *Magnetic Resonance in Medicine 45*, 4 (2001), 580–587. 1

[JBB*12] JENKINSON M., BECKMANN C. F., BEHRENS T. E., WOOLRICH M. W., SMITH S. M.: FSL. *NeuroImage 62*, 2 (2012), 782 – 790. 4

[JVO*07] JIAN B., VEMURI B. C., ÖZARSLAN E., CARNEY P. R., MARECI T. H.: A novel tensor distribution model for the diffusion-weighted MR signal. *NeuroImage 37*, 1 (2007), 164–176. 1, 2

[KVW*09] KUMAR R., VEMURI B. C., WANG F., SYEDA-MAHMOOD T., CARNEY P. R., MARECI T. H.: *Multi-fiber Reconstruction from DW-MRI Using a Continuous Mixture of Hyperspherical von Mises-Fisher Distributions*. Springer Berlin Heidelberg, 2009, pp. 139–150. 1

[LGA*15] LAUMANN T. O., GORDON E. M., ADEYEMO B., SNYDER A. Z., JOO S. J., CHEN M.-Y., GILMORE A. W., MCDERMOTT K. B., NELSON S. M., DOSENBACH N. U., SCHLAGGAR B., MUMFORD J., POLDRACK R., PETERSEN S.: Functional system and areal organization of a highly sampled individual human brain. *Neuron 87*, 3 (2015), 657 – 670. 4

[May13] MAYERHOFER E.: On the existence of non-central wishart distributions. *Journal of Multivariate Analysis 114* (2013), 448–456. 1

[MvZ02] MORI S., VAN ZIJL P. C. M.: Fiber tracking: principles and strategies - a technical review. *NMR in Biomedicine 15*, 7-8 (2002), 468–480. 3

[SA14] SEUNARINE K. K., ALEXANDER D. C.: Chapter 6 - Multiple fibers: Beyond the diffusion tensor. In *Diffusion MRI*, second edition ed. Academic Press, San Diego, 2014, pp. 105 – 123. 4

[SGB*17] SHAKYA S., GU X., BATOOL N., ÖZARSLAN E., KNUTSSON H.: *Multi-fiber Reconstruction using Probabilistic Mixture Models for Diffusion MRI Examinations of the Brain*, vol. In Press. Springer, 2017, ch. 12, pp. –. 1, 2, 4

[TRW*02] TUCH D. S., REESE T. G., WIEGELL M. R., MAKRIS N., BELLIVEAU J. W., WEDEEN V. J.: High angular resolution diffusion imaging reveals intravoxel white matter fiber heterogeneity. *Magnetic Resonance in Medicine 48*, 4 (2002), 577–582. 1

[YPH*06] YUSHKEVICH P. A., PIVEN J., HAZLETT H. C., SMITH R. G., HO S., GEE J. C., GERIG G.: User-guided 3D active contour segmentation of anatomical structures: Significantly improved efficiency and reliability. *Neuroimage 31*, 3 (2006), 1116–1128. 3